Journal of Materials Chemistry A

ROYAL SOCIETY OF CHEMISTRY

PAPER

View Article Online
View Journal | View Issue

Cite this: J. Mater. Chem. A, 2023, 11, 4703

Building-up an interrelationship between isomeric benzyl inner side chains within nonfullerene acceptors and isomeric xylene solvents for non-chlorinated solvent-processed organic solar cells†

Seonghun Jeong,‡[a] Jeewon Park,‡[a] Yutong Ji,‡[c] Yongjoon Cho,[ad] Byongkyu Lee,[ae] Mingyu Jeong,[af] Sungwoo Jung,[a] Sangjin Yang,[a] Youdi Zhang,*[c] Seong-Jun Yoon*[a] and Changduk Yang*[ab]

The side-chain engineering of A–DA'D–A-type nonfullerene acceptors (NFAs), well known as the Y6 series, is an efficient approach for retaining the physical properties of the Y6 series but allowing the manipulation of the solubility, crystallization, intermolecular packing, and orientation. This can permit further fine-tuning of their structures for high power conversion efficiencies (PCEs) of organic solar cells (OSCs). Inspired by recent results regarding the critical roles of "inner side-chain modulation" in the aforementioned features, this study designed and synthesized three isomeric BzY-series NFAs (***o*-BzY**, ***m*-BzY**, and ***p*-BzY**) using *o*-, *m*-, and *p*-hexylbenzyl side chains on the pyrrole motif of the Y6 core framework. This design concept implants a benzene ring at the branching position of the inner side chain. The interrelationship of the isomeric inner side chains within the BzY-series NFAs and isomeric xylene solvents (*o*-, *m*-, and *p*-xylenes) was examined by UV–vis spectroscopy, 1D/2D-nuclear magnetic resonance spectroscopy, and morphological characterization. In-depth studies of 3 (BzY-series NFAs) × 3 (solvents) pair systems of non-chlorinated solvent-processed OSCs found that the best PCEs were achieved from the additive and thermal annealing-free OSCs fabricated with the same structural isomeric pairs of BzY-series NFAs and solvents (*i.e.*, ***o*-BzY** with *o*-xylene, ***m*-BzY** with *m*-xylene, and ***p*-BzY** with *p*-xylene cases). These findings show that the high structural compatibility between the side chains and processing solvents has great potential for improving the OSC performance.

Received 3rd November 2022
Accepted 1st February 2023

DOI: 10.1039/d2ta08621b

rsc.li/materials-a

Introduction

Organic solar cells (OSCs) have attracted considerable attention as one of the next-generation energy harvesting systems owing to their light weight, facile synthesis, low cost, and easily tunable optoelectronic properties. Extensive advances have been achieved through innovations in both device engineering and material design for over 30 years.[1–6] In particular, tremendous improvement in the power conversion efficiencies (PCEs) of OSCs has been made by the emergence of nonfullerene acceptors (NFAs), which enable long-wavelength absorption and low energy loss.[7–10] Y6 is one of the state-of-the-art NFAs first reported by Zou *et al.* in 2019.[11] After surpassing 15% PCE using a Y6 NFA with a PM6 donor polymer, many molecular structural modifications were performed. The development of the so-called Y-series NFAs has induced a renaissance in OSCs with a record PCE beyond 19% based on single-junction OSCs.[12,13]

Y-series NFAs consist of an A–DA′D–A-type π-backbone and two sets of alkyl side chains located on the "outer position" at the 2-position of the thienothiophene moieties and the "inner position" at the pyrrole rings (see Fig. 1). One approach for developing new Y-series NFAs is modifying the π-backbone core. Several attempts have been made for π-framework variation, including changing the heteroatom of the core DA′D structure, modulating the π-extension of fused rings, and

[a]School of Energy and Chemical Engineering, Perovtronics Research Center, Low Dimensional Carbon Materials Center, Ulsan National Institute of Science and Technology (UNIST), 50 UNIST-gil, Ulju-gun, Ulsan 44919, South Korea. E-mail: yang@unist.ac.kr; yoonsj@unist.ac.kr

[b]Graduate School of Carbon Neutrality, Ulsan National Institute of Science and Technology (UNIST), 50 UNIST-gil, Ulju-gun, Ulsan 44919, South Korea

[c]College of Chemistry, Key Laboratory of Advanced Green Functional Materials, Changchun Normal University, Changchun 130032, China. E-mail: zhangyd@ccsfu.edu.cn

[d]Department of Chemistry and Materials Research Center, Northwestern University, 2145 Sheridan Road, Evanston, IL 60208, USA

[e]Department of Physics and Organic and Carbon Electronics Laboratories (ORaCEL), North Carolina State University, Raleigh, NC 27695, USA

[f]KEPCO Research Institute, Korea Electric Power Corporation, 105, Munji-ro, Yuseong-gu, Daejeon 34056, Republic of Korea

† Electronic supplementary information (ESI) available. See DOI: https://doi.org/10.1039/d2ta08621b

‡ These authors contributed equally.

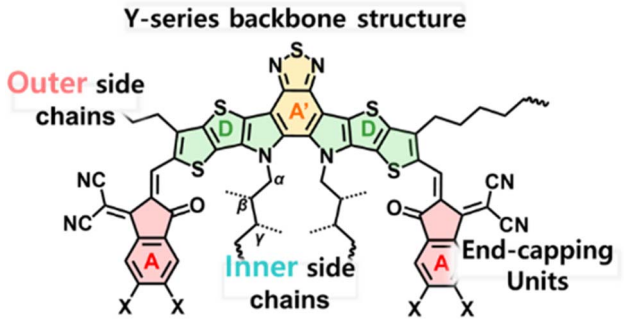

Fig. 1 Chemical structure of A–DA′D–A structured BTP backbone-based small molecule acceptors.

attaching different end-capping units.[14–16] This modulation simultaneously influences the intrinsic molecular electronic properties (such as the absorption spectrum and energy level) and intermolecular interactions. Another efficient approach for advances in Y-series NFAs is alkyl side-chain alternation, which primarily affects intermolecular interactions. Surprisingly, this alkyl side-chain engineering effectively modulates the morphology, molecular ordering, phase separation, and mixing. This can be a powerful method of optimizing the molecular design of Y-series NFAs for high-performance OSCs. On the outer position at the 2-position of the thienothiophene moieties in Fig. 1, various modifications, including alkyl chain length variation, branched alkyl side-chain alteration, and alkylaryl-group introduction, have enhanced the performance of OSCs.[8,17,18] In the case of the inner position at the pyrrole rings (see Fig. 1), introducing a branched alkyl side chain is essential for achieving high PCEs. The attachment of linear alkyl side chains into the inner position of Y-series NFAs could lead to limited solubility of the resulting NFAs in various processing solvents, even though the outer alkyl side chains are branched, thereby worsening the OSC performance.[19] Therefore, it is essential to maintain the branched inner side chains when designing high-performance Y-series NFAs. For example, β- and γ-branched inner side chain-containing Y-series NFAs are an archetype of the state-of-the-art Y-series NFAs.[19] In addition to high PCE, there is another critical factor that needs to be considered for the successful commercialization of OSCs. A process safety issue during device fabrication is caused by the use of harmful chlorinated organic solvents, such as chloroform (CF) and chlorobenzene (CB).[20–22] Recently, new Y-series NFAs that can be used with non-chlorine solvents were developed by appropriately controlling the solubility and blend morphologies. Huang *et al.* reported a high-performing NFA, DTY6, designed by extending the branched inner alkyl side-chain length that achieved a high PCE of more than 16% in a non-chlorinated solvent (*o*-xylene) processing system.[23] Kim *et al.* reported the outer side chain-tuned selenophene-incorporated Y6 analogs demonstrating a PCE of 16.11% with an *o*-xylene processing solvent.[14] Nevertheless, most attempts to obtain the constitutional ideality of Y-series NFAs toward non-chlorinated solvent-processed OSCs are still limited to modulating the linear or branched alkyl side-chain lengths.

This paper introduces hexylbenzyl inner side chains into the Y6 core structure to give distinctive features as a new approach for inner side-chain engineering. Three new isomeric Y-series NFAs are presented, called ***o*-BzY**, ***m*-BzY**, and ***p*-BzY** (so-called BzY-series NFAs), which are incorporated with three isomeric benzyl alkyl side chains (*o*-, *m*, and *p*-hexylbenzyl groups) into the inner position of the Y6 core structure. These new isomeric Y-series NFAs were applied to OSCs with three isomeric xylenes (*o*-, *m*-, and *p*-xylenes) as non-chlorinated processing solvents. The BzY-series NFAs had sufficient solubility in these non-chlorinated xylene solvents for the fabrication of OSCs. Therefore, this study explored the interrelationship between the isomeric benzyl inner sides of BzY-series NFAs and isomeric non-chlorinated xylene solvents (*o*-, *m*-, and *p*-xylenes) using a combination of one-/two-dimensional nuclear magnetic resonance (1/2D-NMR) spectroscopy and in-depth optical studies. Interestingly, all the BzY-series NFA-based devices with PM6 donor polymer showed their optimal PCEs without the need for additives or thermal annealing. A more interesting discovery was that the structurally identically oriented pairs of BzY-series NFA and xylene (*i.e.*, ***o*-BzY** with *o*-xylene, ***m*-BzY** with *m*-xylene, and ***p*-BzY** with *p*-xylene)-based OSCs yielded superior photovoltaic performance, compared to the corresponding other pair systems. Furthermore, the PM6 : ***m*-BzY**-based device prepared with *m*-xylene showed the highest PCE of 16.1%, which is almost equal to the highest PCE of OSCs with a non-additive, non-annealing process, and non-chlorinated solvent reported in the literature (*vide infra*). This paper reports the novel design strategy of Y-series NFAs for realizing practical OSCs with a non-chlorinated solvent, non-additive, and non-thermal annealing process. In addition, it provides a reference for understanding the structure–processing solvent–property relationship.

Results and discussion

Material design, synthesis, and characterization

Implanting a benzene ring at the branching position of the inner side chain in Y-series NFAs would induce unique features because the intrinsic properties of the 2D aromatic side chains (*e.g.*, bulkiness and rigidity) are very different from those of alkyl side chains. Scheme 1 outlines the chemical structures and synthetic routes of Y-series NFAs, and the ESI† details the synthetic procedures. First, the Grignard reaction of three isomeric bis(bromomethyl)benzene compounds and 1-bromopentane using a copper(I) bromide dimethyl sulfide complex as a catalyst was conducted to synthesize the *o*-, *m*-, and *p*-hexylbenzyl bromides (**1a**, **1b**, and **1c**). 5,6-Dinitro-4,7-bis(6-undecylthieno[3,2-*b*]thiophen-2-yl)benzo[*c*][1,2,5]thiadiazole (**2**) was synthesized *via* palladium-catalyzed Stille coupling using $Pd(PPh_3)_4$ as the catalyst in anhydrous toluene. The benzyl inner side-chain-containing fused DA′D cores (**3a**, **3b**, and **3c**) were prepared by Cadogan cyclization, which then converted the corresponding dialdehyde intermediates (**4a**, **4b**, and **4c**) *via* the Vilsmeier–Haack reaction. Finally, the three new isomeric BzY-series NFAs, ***o*-BzY**, ***m*-BzY**, and ***p*-BzY**, were afforded by the Knoevenagel condensation of each dialdehyde compound with

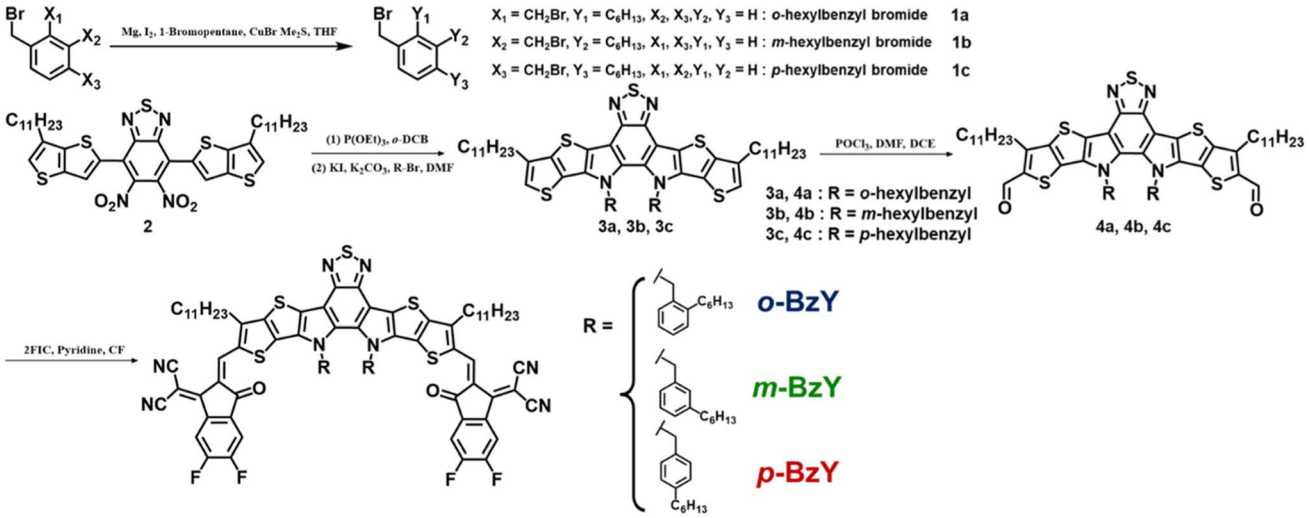

Scheme 1 Chemical structures and synthetic routes of *o*-BzY, *m*-BzY, and *p*-BzY.

the end-capping unit, 2FIC, under pyridine-catalyzed conditions. The chemical structures of the intermediates and final target molecules were fully characterized by ^{1}H and ^{13}C NMR spectroscopy (see the Experimental section and ESI†). All the synthesized NFAs showed good solubility in all the used xylenes at 80 °C, as well as common chlorine solvents at room temperature (Fig. S1†). In addition, thermogravimetric analysis (TGA) showed that these NFAs have good thermal stability with a thermal decomposition temperature (T_d) with 5% weight loss at 302 °C for ***o*-BzY**, 296 °C for ***m*-BzY**, and 292 °C for ***p*-BzY** (Fig. S2† and Table S1†).

Theoretical calculations and physicochemical properties

Density functional theory (DFT) calculation using a B3LYP/6-31G(d,p) basis set was performed on the ***o*-BzY**, ***m*-BzY**, and ***p*-BzY** molecules to investigate the isomeric structural effect of the inner side chains on the electron density distribution, molecular dipole moment, and optimized molecular conformation (Fig. 2(a)–(c) and S3†). In the optimized geometries, the torsion angles between the central core unit and the end-capping unit (2FIC) were different depending on the three benzylic side chains; ***o*-BzY** had slightly larger torsion angles of 2.41° and 2.42° compared to ***m*-BzY** (1.90° on both sides) and ***p*-BzY** (1.91°

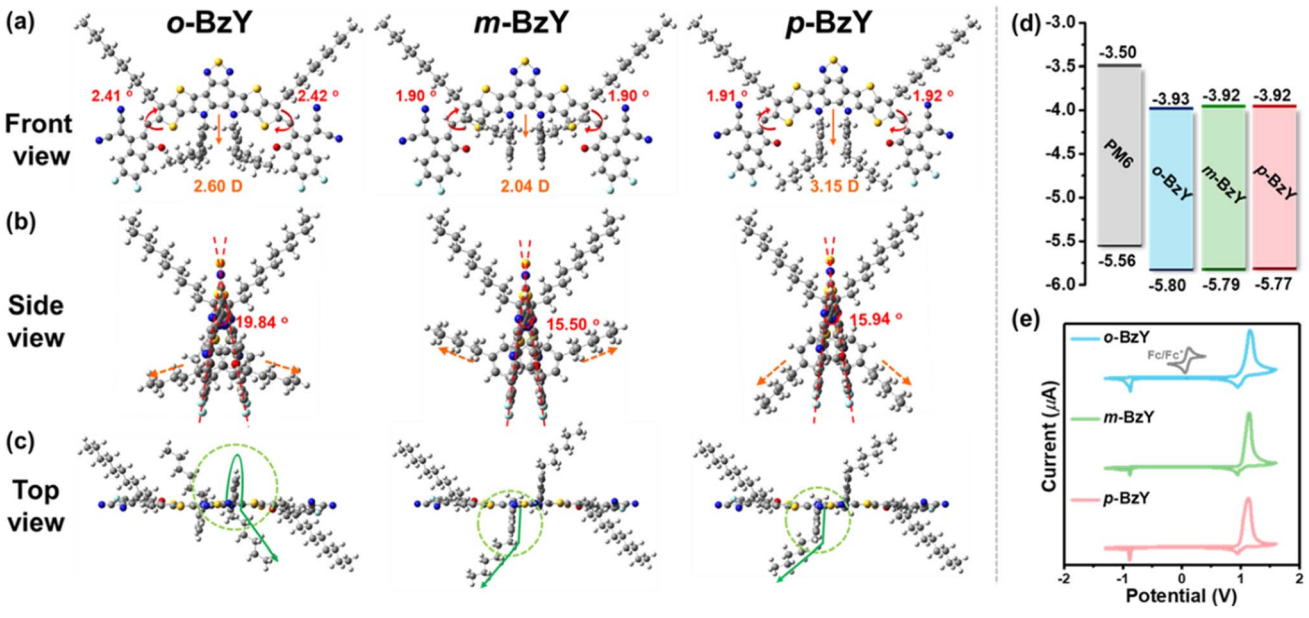

Fig. 2 (a) Front view, (b) side view, and (c) top view of BzY-series NFAs in optimized molecular geometries (dashed arrows represent the local dipole direction of hexylbenzene). (d) Energy level diagrams of PM6 and BzY-series NFAs. (e) Cyclic voltammetry of BzY-series NFAs.

and 1.92°) (Fig. 2(a)). Furthermore, as shown in Fig. 2(b), ***o*-BzY** exhibited a considerably higher twisted angle of 19.84° between the two planes made up of 2FIC units in each terminal position and the central 2,1,3-benzothiadiazole unit, while ***m*-BzY** and ***p*-BzY** had smaller values of 15.50° and 15.94°, respectively. These different geometries in the ***o*-BzY** molecule are probably due to the different geometric locations of the benzyl pendant on the BzY-series acceptor. From the top view of the molecules (Fig. 2(c)), the benzene rings protrude in a vertical direction relative to the molecular plain in the cases of ***m*-BzY** and ***p*-BzY**, which is slightly different from those of ***o*-BzY**. The benzene rings were located on the ***o*-BzY** molecule with less protruded geometry because of the *ortho*-position hexyl moiety on the benzyl pendant; thus, the steric effect of the benzyl pendant induces more twisted geometry on the backbone of the ***o*-BzY** molecule. This suggests that utilizing the *m*- and *p*-hexylbenzyl side chains of the inner N-sites in Y6 analogs promotes higher molecular planarity and intermolecular π–π interactions, which is consistent with the trend of the changed optical profiles, in which compared to ***o*-BzY**, more red-shifted absorption of ***m*-BzY** and ***p*-BzY** is observed from the solution to the thin-film state compared (*vide infra*).[24] In addition, the isomeric effect in the benzyl side chain made a slight difference in the molecular dipole moment in the optimized geometries of NFAs. This dipole moment variation is related to the direction and location of the hexyl moiety in the benzyl pendant of the inner side-chain position of the BzY-series NFAs. From the front and side views of Fig. 2, the total dipole moment of the whole molecule increases (order: ***p*-BzY** (3.15 D), ***o*-BzY** (2.60 D), and ***m*-BzY** (2.04 D), see Table S2† for the vector values) when the hexyl moiety is toward the vertical direction and located downward. To support the understanding of this phenomenon, the local dipole of hexylbenzene constituting inner benzyl side chains was calculated.[25,26] As illustrated in Fig. S4,† the hexylbenzene had a local dipole of 0.3776 D with the direction in which the hexyl moiety stretched. It implies that the dipole moment of BzY-series NFAs with hexyl chains extending downward can be increased (see Fig. 2(b) for the local dipole direction of the hexylbenzene unit in the molecular geometry of each BzY-series NFA). The isomeric xylene solvents also exhibit different dipole moments (*o*-xylene (0.59 D), *m*-xylene (0.31 D), and *p*-xylene (0.08 D) from the DFT calculation with the same basis set) depending on the isomeric structure, so the slight differences in dipole moment on both isomeric NFAs and xylenes probably would affect subtle intermolecular interaction behaviors.[27] As shown in Fig. S3,† the highest occupied molecular orbital (HOMO) wave functions were localized mainly on the central electron-donating core units. In contrast, the lowest unoccupied molecular orbitals (LUMOs) were well-delocalized along the molecular backbones, implying the n-type character of synthesized NFAs and representing efficient intramolecular charge transfer behavior.[28] In addition, the calculated HOMO/LUMO energy levels are −5.51/−3.48, −5.50/−3.46, and −5.49/−3.47 eV for ***o*-BzY**, ***m*-BzY**, and ***p*-BzY**, respectively. As expected, the isomerism in the benzyl alkyl chains as the inner side-chain rarely affects the intrinsic electronic properties of the BzY-series NFAs in an isolated state from the calculation results.

The experimental electrochemical properties were examined by cyclic voltammetry (CV) to evaluate the HOMO and LUMO levels of BzY-series NFAs (Fig. 2(d) and (e) and Table 1) using ferrocene/ferrocenium (Fc/Fc^+) as the external standard. As shown in Fig. 2(d), ***o*-BzY**, ***m*-BzY**, and ***p*-BzY** have similar HOMO/LUMO levels of −5.80/−3.93, −5.79/−3.93, and −5.76/−3.92 eV, respectively.[29,30] Additionally, we carried out ultraviolet photoelectron spectroscopy to compare the HOMO levels of NFAs with the CV and DFT results.[31,32] As provided in Fig. S5,† BzY-series NFAs have similar HOMO energy levels of −5.63 for ***o*-BzY**, −5.58 for ***m*-BzY**, and −5.60 for ***p*-BzY**. It indicates that three isomeric benzyl side chains do not endow conspicuous effects on the energy levels of the BzY-series NFAs.[17]

Intermolecular interaction behaviors of BzY-series NFAs depending on isomeric xylene solvents

The correlation between isomeric benzyl inner side chains and isomeric xylene solvents was assessed by analyzing the optical, morphological, and structural characteristics of the BzY-series NFA solutions and thin films using isomeric xylenes, respectively. Ultraviolet–visible (UV–vis) absorption spectroscopy was conducted (Fig. 3 and Table 1) to assess the optical properties of

Table 1 Optical and electrochemical properties of *o*-BzY, *m*-BzY, and *p*-BzY

NFAs	Processing solvent	λ_{sol}^{max} [nm][a]	λ_{film}^{max} [nm][a]	λ_{onset} [nm][b]	E_g^{opt} [eV][b]	E_{HOMO}^{CV} [eV][c]	E_{LUMO}^{CV} [eV][c]
***o*-BzY**	*o*-Xylene	720	769	829	1.50	−5.80	−3.93
	m-Xylene	718	754	820	1.51		
	p-Xylene	717	755	816	1.52		
***m*-BzY**	*o*-Xylene	721	791	857	1.45	−5.79	−3.92
	m-Xylene	719	794	859	1.44		
	p-Xylene	718	792	858	1.45		
***p*-BzY**	*o*-Xylene	721	782	854	1.45	−5.77	−3.92
	m-Xylene	718	783	856	1.45		
	p-Xylene	718	781	854	1.45		

[a] Taken from the material solutions in xylenes and corresponding films on glass substrates. [b] Determined from the onset of the UV-vis absorption plots in the films. [c] Estimated from the oxidation and reduction onset by using the equations of $E_{HOMO} = -(E_{ox}^{onset} - E_{Fc}^{onset} + 4.8)$ eV, $E_{LUMO} = -(E_{red}^{onset} - E_{Fc}^{onset} + 4.8)$ eV, and $E_g^{CV} = E_{HOMO} - E_{LUMO}$.

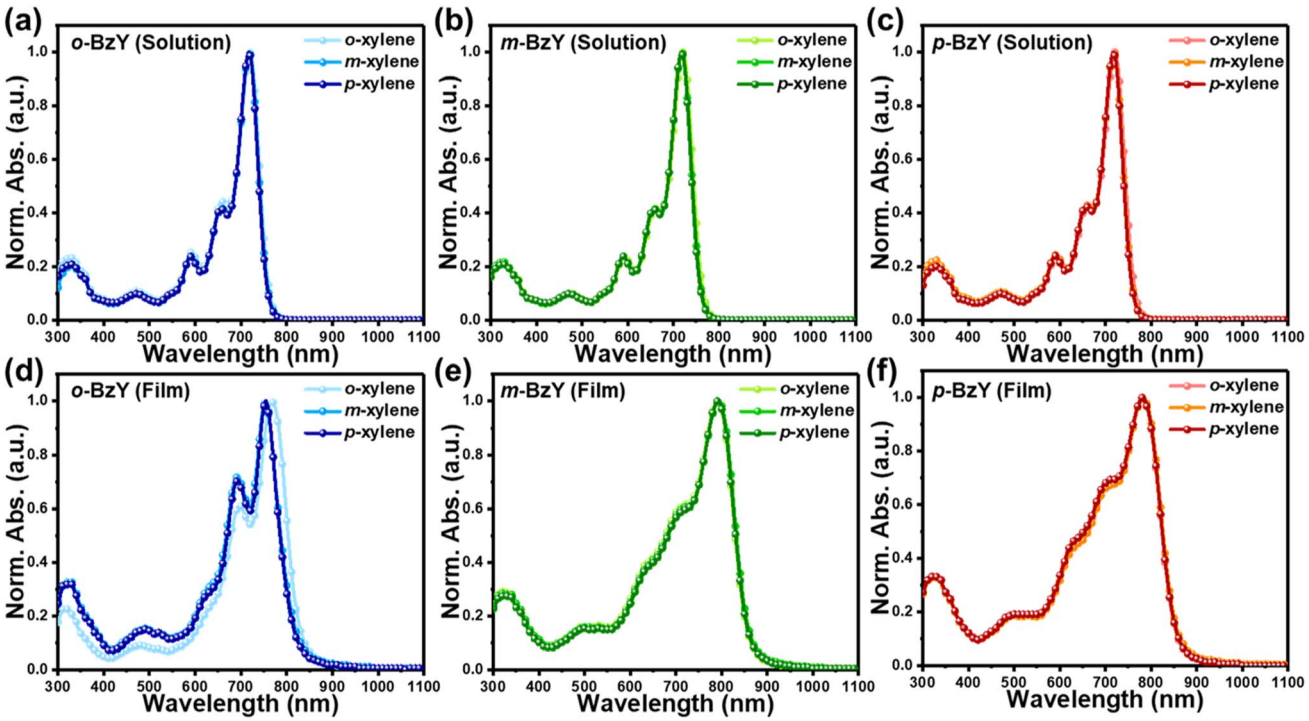

Fig. 3 (a)–(c) Normalized UV-vis absorption spectra in each xylene solution and (d)–(f) corresponding thin film of ***o*-BzY**, ***m*-BzY**, and ***p*-BzY**.

***o*-BzY**, ***m*-BzY**, and ***p*-BzY** in each of the *o*-, *m*-, and *p*-xylenes and corresponding thin-film states. As shown in Fig. 3(a)–(c), in dilute *o*-, *m*-, and *p*-xylene solutions, the three BzY-series NFAs showed similar absorption spectra and strong absorption in the 500–800 nm range with maximum absorption peaks (λ_{max}s) at 718–721 nm in each solvent, indicating that both the isomeric benzyl side chains and the isomeric xylene solvents had no isomeric structural effect on the absorption ranges of the BzY-series NFAs in the solution states. It is attributed to the similar polarities of isomeric xylenes and the negligible effect of the isomeric benzyl side chains on the conjugation length/intramolecular charge transfer of the BzY-series NFAs in the solution states.[8,17,33] In addition, the temperature-dependent absorption of BzY-series NFAs was measured to reveal the aggregation behaviors in the solution state. As shown in Fig. S6,† all BzY-series NFAs displayed temperature-dependent aggregation tendencies with weakened peak intensity over elevated temperatures. This indicates the preaggregation features of BzY-series NFAs in xylene solutions.[34,35] In particular, ***p*-BzY** showed slightly higher temperature-dependent aggregation properties in *p*-xylene than the *o*- and *m*-xylene solutions, which is probably due to the relatively lower compatibility of ***p*-BzY** with *p*-xylene of the low dipole moment of 0.08 D (0.31 D for *m*-xylene and 0.59 D for *o*-xylene).[36] Furthermore, in terms of the degree of the solvatochromic shift estimated by comparing the λ_{max}s of the synthesized BzY-series NFAs in the *p*-xylene and CF solutions, which were selected as nonpolar and polar solvents, respectively (Fig. S7 and Tables S3 and S4†), the different hexyl-attached positions in the benzyl side chain affect the polarity of the molecular excited state; ***p*-BzY** showed a slightly higher $\Delta\nu$ of 229 cm^{-1} compared to ***m*-BzY** and ***o*-BzY** ($\Delta\nu = 211\ cm^{-1}$), which was attributed to the larger dipole moment of ***p*-BzY** and well matched with the DFT calculation results above.[36]

When changing from the solution to thin-film states (Fig. 3(d)–(f)), ***m*-BzY** consistently showed slightly larger red-shifted absorption profiles with λ_{max} values of 791–794 nm compared to ***p*-BzY** (λ_{max} of 781–783 nm) and ***o*-BzY** (λ_{max} of 754–769 nm) in all the used xylene-processed films. This indicates that the position of substituted hexyl chains on the benzyl ring affects the intermolecular packing; particularly the *m*-substituted hexyl benzyl side chain induces larger intermolecular π–π interaction among the BzY-series NFAs.[32] Intriguingly, ***o*-BzY** displayed more pronounced shoulder peaks at around 690 nm, probably due to the different aggregation tendency with higher intermolecular ordering than the other two isomeric NFAs.[37] Furthermore, the absorption spectrum of ***o*-BzY** exhibited a more red-shifted phenomenon in an *o*-xylene-processed film than in *m*-xylene- or *p*-xylene-processed films (λ_{max} of 769 nm in *o*-xylene-, 754 nm in *m*-xylene-, and 755 nm in *p*-xylene-coated films, respectively), inferring different intermolecular π–π interactions depending on the isomeric xylenes during film formation. The absorption spectrum of ***p*-BzY** displayed a slightly higher 0–1 shoulder peak than ***m*-BzY**, suggesting different aggregation behaviors between ***m*-BzY** and ***p*-BzY**. In addition, as shown in Fig. S8,† the absorption coefficients of thin films of the BzY-series NFAs prepared from three types of isomeric xylene were measured. In particular, ***o*-BzY** films demonstrated slightly lower values than ***m*-BzY** and ***p*-BzY** despite the higher aggregation properties. It probably originated from different packing behaviors induced by inner side-chain orientation. Among them, *o*-xylene-processed film showed a higher value of approximately $1.25 \times 10^5\ cm^{-1}$ than the *m*-xylene and *p*-xylene-processed ones

because of the enhanced intermolecular π–π interactions. Hence, the hexyl-substituted position on the inner benzyl alkyl and the processing solvents influence the molecular packing in the thin-film state.

The isomeric effects of the BzY-series NFAs and xylene solvents on nanoscale morphologies were confirmed by measuring the corresponding films using atomic force microscopy (AFM) and grazing-incident wide-angle X-ray scattering (GIWAXS). Compared to other films, all the ***o*-BzY** films showed rougher surface morphologies with high root-mean-square (RMS) values of 8.26–21.7 nm, arising from the stronger aggregation and intermolecular ordering during the film forming process (Fig. 4(a)). In particular, the *m*-xylene-processed ***o*-BzY** film showed a significantly higher RMS value of 21.7 nm than the corresponding *o*-xylene- and *p*-xylene-processed ones owing to compact aggregation during the film-formation process. In *m*-xylene- and *p*-xylene-processed ***m*-BzY** films, slightly rougher surface morphologies with higher RMS roughness values of 3.92–4.35 nm were observed compared to the corresponding *o*-xylene-processed film. This indicates that more compact aggregation of ***m*-BzY** occurred in *m*-xylene- and *p*-xylene-processed films during the film-formation process because of the better solubility originating from relatively lower intermolecular interaction than in *o*-xylene. In contrast, all the ***p*-BzY** exhibited a very smooth surface with RMS values of 0.404–0.421 nm and no significant differences in the RMS value among the three kinds of xylene-processed films. The isomeric BzY-series NFAs displayed significantly different diffraction peaks in the results of GIWAXS measurement, as illustrated in Fig. 4(b), S9 and summarized in Table S5†. First, ***o*-BzY** films exhibited a polycrystalline feature with many crystallites distributed along large azimuthal angles independently of the processing solvent because of the highly ordered crystallites, strong molecular aggregation, random crystal orientation, and the presence of multiple polymorphs.[38] The ***m*-BzY** and ***p*-BzY** neat films commonly exhibited preferential face-on orientation, similar to other reported Y6-derivatives.[11,18] Generally, all the ***m*-BzY** showed denser intermolecular packing with small d-spacing values of 3.634–3.675 Å in the out-of-plane (OOP) direction than ***p*-BzY** (3.668–3.714 Å), due to the stronger intermolecular π–π stacking. In particular, in the *p*-xylene-processed film, the ***m*-BzY** film had another lamellar stacking peak along the in-plane (IP) direction at $q_{xy} = 0.197$ Å^{-1}, indicating different molecular packing structures depending on the processing solvents (see Fig. 4(b)). The most characteristic point in the ***p*-BzY** neat films was the strong π–π stacking peaks in the OOP direction containing distinct tilted signals in the small azimuthal angle range originating from the tilted intermolecular packing structure toward the substrates (see Fig. 4(b)). In the *p*-xylene-processed ***p*-BzY** film, an additional strong lamellar stacking peak was observed along the OOP direction at $q_z = 0.422$ Å^{-1}, indicating the coexistence of an edge-on orientation (Fig. 4(b)).[39] The slightly different molecular packing orientations of *p*-xylene-processed ***m*-BzY** and ***p*-BzY** films compared to other films processed with *o*-xylene and *m*-xylene probably originated from partial interactions of BzY-series NFAs in xylene solution (*vide infra*) and different physical properties of xylenes which can determine the kinetics in the film forming process (Table S6†). The calculated crystalline coherence length (CCL) estimated using the Scherrer equation showed that ***m*-BzY** has a higher crystalline feature along the OOP direction than ***p*-BzY**, which benefits vertical charge transport. Moreover, the *m*-xylene- and *p*-xylene-processed ***m*-BzY** films had relatively higher CCL values in both the IP and OOP directions than the *o*-xylene-processed ones, reconfirming the enhanced aggregation

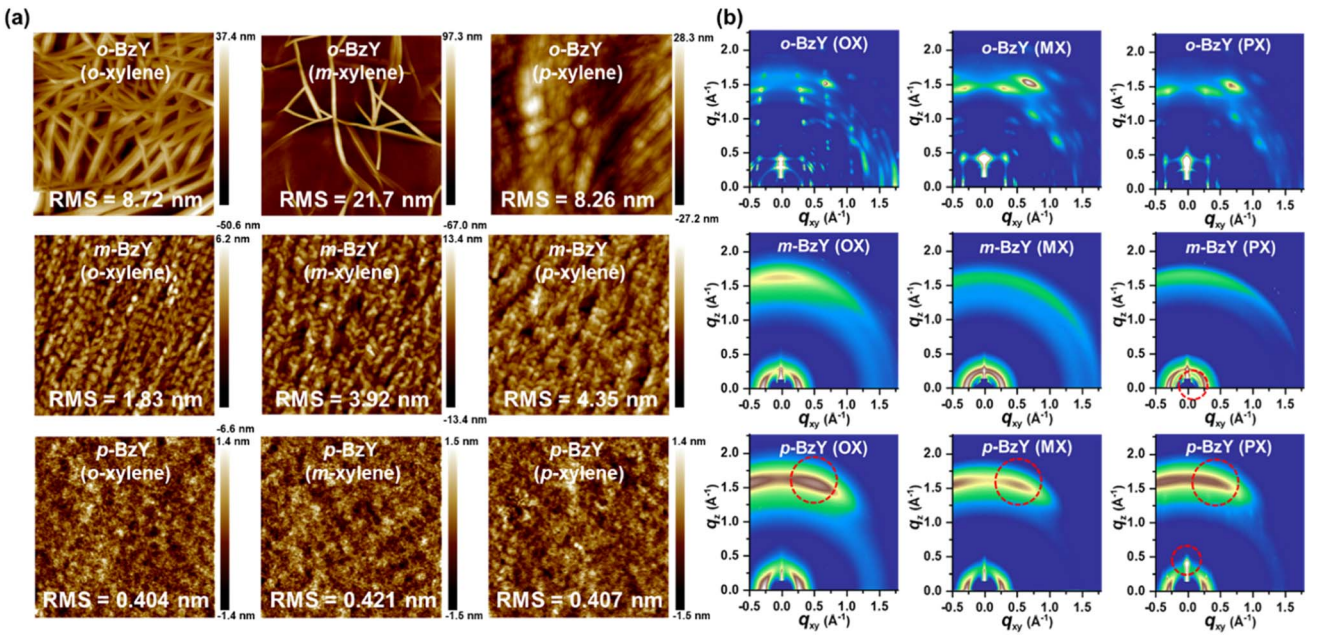

Fig. 4 (a) AFM images and (b) 2D GIWAXS images of BzY-series NFA neat films prepared with three types of xylenes: *o*-xylene (OX), *m*-xylene (MX), and *p*-xylene (PX).

properties grown during the film-formation process of the ***m*-BzY** films fabricated with *m*-xylene and *p*-xylene solvents (Table S5†).

NMR spectroscopy for investigating the interrelationship between the BzY-series molecules and xylene solvents

1D- and 2D-diffusion-ordered spectroscopy (DOSY)-mode NMR with deuterated CF and xylene solvents (*i.e.*, $CDCl_3$, *o*-xylene-d_{10}, *m*-xylene-d_{10}, and *p*-xylene-d_{10}) were performed to further explore the origins of the interrelationship between isomeric BzY-series NFAs and isomeric xylene solvents (Fig. 5 and S10†). Four well-distinguishable peaks were observed in the NMR spectrum of molecules that represent the vinyl linkage (H_1), end-capping group (H_2), inner side-chain (H_3), and outer side-chain (H_4). These peaks were assessed to observe the change in the chemical environment of the molecules depending on the solvents and temperatures. As shown in Fig. 5(a), ***o*-BzY** showed distinct differences in chemical shifts between room temperature and elevated temperatures in all deuterated solvents used compared to ***m*-BzY** and ***p*-BzY**. In the $CDCl_3$ solutions, the change in the chemical shifts of H_1 (0.07 ppm) in ***o*-BzY** between

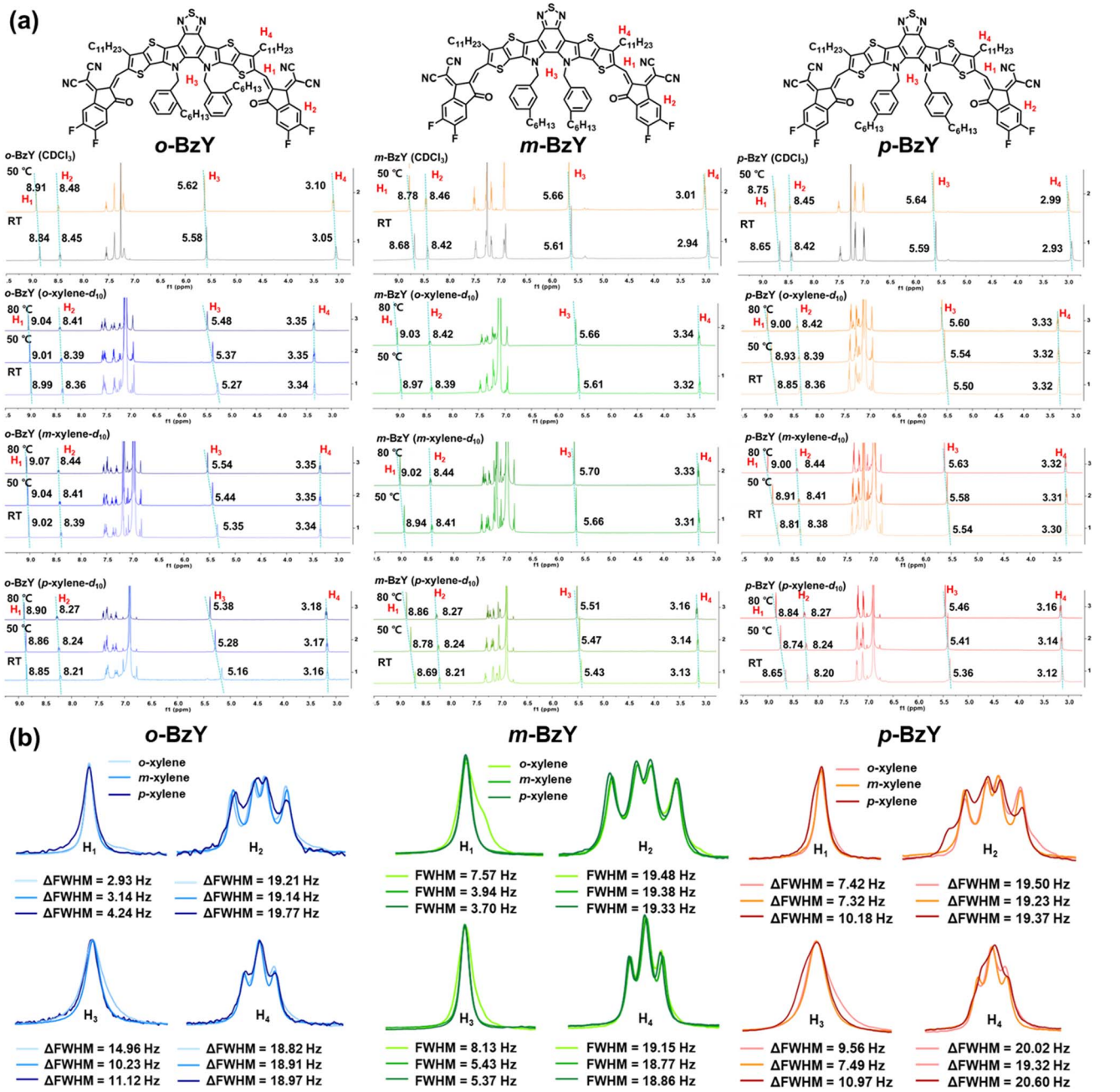

Fig. 5 (a) Chemical shift of H_1–H_4 of BzY-series acceptors at elevated temperatures in $CDCl_3$, *o*-xylene-d_{10}, *m*-xylene-d_{10}, and *p*-xylene-d_{10}. (b) FWHM values of H_1–H_4 of ***o*-BzY** and ***p*-BzY** at room temperature and ***m*-BzY** at 50 °C.

room temperature and 50 °C was smaller than that in ***m*-BzY** (0.10 ppm) and ***p*-BzY** (0.10 ppm), whereas there were similar differences in the change in other assigned peaks (H_2, H_3, and H_4) when the samples were heated to 50 °C. This indicates that ***o*-BzY** maintained a higher degree of aggregation than ***m*-BzY** and ***p*-BzY** even at 50 °C. Interestingly, in deuterated xylenes systems, ***o*-BzY** had a more dramatic contrast. As summarized in Table S7†, ***o*-BzY** exhibited smaller changes in chemical shifts of approximately 0.02–0.04 ppm in H_1 (concerned with the vinyl linkage) than ***m*-BzY** (0.06–0.09 ppm) and ***p*-BzY** (0.07–0.10 ppm) with increasing temperature. Importantly, it had contrastively dramatic chemical shift differences of 0.09–0.12 ppm in H_3 (related to the inner side-chain) of ***o*-BzY** compared to ***m*-BzY** (0.04–0.05 ppm) and ***m*-BzY** (0.04–0.06 ppm) under the increased measured temperature. This suggests that intermolecular interaction and aggregation of ***o*-BzY** were affected mainly by the inner side-chain, and the different geometric locations of the benzyl pendant of ***o*-BzY** induced characteristic partial intermolecular behaviors, unlike ***m*-BzY** and ***p*-BzY**. Furthermore, the broadness of each peak, full-width at half maximum (FWHM), was compared to investigate the effect of xylene solvents on the partial intermolecular interaction (see Fig. 5(b)). All the BzY-series NFAs showed similar peak broadness in H_2 and H_4, suggesting that the kinds of solvents cannot significantly affect the intermolecular interactions associated with the end-capping units and outer side chains. In the case of ***o*-BzY**, however, the peak of H_1 in the *p*-xylene-d_{10} solution (FWHM of 4.24 Hz) was more than 1.35 times broader than those in *o*-xylene-d_{10} (FWHM = 2.93 Hz) and *m*-xylene-d_{10} (FWHM = 3.14 Hz) solutions, and the peak of H_3 in *o*-xylene-d_{10} solution showed a more than 1.35 times higher broadness than those in the other isomeric xylene-d_{10} solutions. Hence, each partial interaction of vinyl linkages and inner side chains dominantly works for the intermolecular interaction of ***o*-BzY** in *p*-xylene and *o*-xylene, respectively.[40] Furthermore, ***m*-BzY** in the *o*-xylene-d_{10} solution and ***p*-BzY** in the *p*-xylene-d_{10} solution exhibited much broader H_1 and H_3 peaks than those in the other deuterated xylene solvents, respectively, indicating the slightly stronger partial intermolecular interaction of vinyl linkages and inner side chains in each solvent.

DOSY NMR experiments were also carried out to investigate the intermolecular interactions. The diffusion coefficient (D) is related to intermolecular interactions and aggregations.[41] As depicted in Fig. S10† and summarized in Table S8†, ***o*-BzY** in *m*-xylene-d_{10} had higher D values in H_1–H_4 than *o*-xylene-d_{10} and *p*-xylene-d_{10} solutions, indicating suppressed partial intermolecular interactions.[42,43] At the same time, ***o*-BzY** in *o*-xylene-d_{10} had lower D values in H_1–H_4 than *m*-xylene-d_{10} and *p*-xylene-d_{10} solutions, demonstrating higher intermolecular interactions in *o*-xylene solution. It can be considered one of the reasons for the difference in the UV-vis absorption spectra of ***o*-BzY** films depending on the kind of processing isomeric xylene solvent (*vide supra*). Also, ***p*-BzY** exhibited slightly lower D values in H_1–H_4 compared to ***o*-BzY** in each deuterated xylene solvent. It can be inferred that higher partial intermolecular interaction of ***p*-BzY** with lower D values is one of the origins of the largely red-shifted absorption band of ***p*-BzY** films compared to ***o*-BzY** films. Especially, ***p*-BzY** exhibited even lower D values in the *p*-xylene-d_{10}-solutions, implying higher intermolecular interaction in the *p*-xylene system, which is consistent with the analysis of the aforementioned 1D-NMR peak broadness. Consequentially, an analysis of 1/2D-NMR spectroscopy strongly shows that the isomeric inner benzyl side chains affect different intermolecular behaviors in the solution state. Moreover, the kinds of isomeric xylene solvents can also induce different partial intermolecular interactions.

Photovoltaic performance and energy loss analysis

OSCs based on three isomeric BzY-series NFAs and xylenes were fabricated with a conventional device structure of indium-tin-oxide (ITO)/poly(3,4-ethylenedioxythiophene):poly(styrenesulfonate) (PEDOT:PSS)/PM6:NFAs/PDINO/Al to investigate the effects of the relationship mentioned above between NFAs and processing solvents on the device performance. The representative polymer PM6 was selected as a donor because the energy level is well matched with those of the NFAs, and the complementary absorption is maintained correctly.[44] The optimal blend ratios of PM6 : ***o*-BzY** (D/A 1 : 1.5), PM6 : ***m*-BzY** (D/A 1 : 1.3), and PM6 : ***p*-BzY** (D/A 1 : 1.2 wt.) were found by varying the ratio of the active layer materials (Table S9†). The donor/acceptor blends were dissolved in the three isomeric xylene solvents. The devices with an as-cast active layer showed optimal performance without any additive and thermal annealing, which provides the usefulness of the BzY-series NFAs toward realizing cost-effective and simply processable OSCs.[45,46] Fig. 6(a)–(c) show the representative current density–voltage (J–V) curves of the devices measured under simulated AM1.5G one-sun illumination (100 mW cm^{-2}), and Table 2 lists the detailed photovoltaic parameters. Among them, the as-cast device of PM6 : ***m*-BzY** processed with *m*-xylene yielded a high PCE of 16.1% with an open-circuit voltage (V_{OC}) of 0.888 V, short-circuit current density (J_{SC}) of 24.4 mA cm^{-2}, and fill factor (FF) of 74.5%. Under the conditions of *o*-xylene and *p*-xylene, however, the PCEs decreased to 15.2% (V_{OC} of 0.881 V, J_{SC} of 23.2 mA cm^{-2}, and FF of 74.3%) and 13.6% (V_{OC} of 0.886 V, J_{SC} of 21.3 mA cm^{-2}, and FF of 72.2%), respectively. The PM6 : ***p*-BzY** device fabricated with *p*-xylene showed a higher PCE of 15.4% with a V_{OC} of 0.891 V, J_{SC} of 24.2 mA cm^{-2}, and FF of 71.3% compared to the slightly inferior PCEs of 13.6% (V_{OC} of 0.888 V, J_{SC} of 22.6 mA cm^{-2}, and FF of 67.9%) and 14.4% (V_{OC} of 0.878 V, J_{SC} of 23.9 mA cm^{-2}, and FF of 68.5%) for the *o*-xylene and *m*-xylene-processed devices, respectively. In addition, the PM6 : *o*-BzY-based OSC prepared with *o*-xylene showed a moderate PCE of 14.2% (V_{OC} of 0.924 V, J_{SC} of 22.7 mA cm^{-2}, and FF of 67.9%), which is higher than the efficiencies achieved in the *m*-xylene and *p*-xylene-processed devices (PCEs of 10.2% with a V_{OC} of 0.935 V, J_{SC} of 20.0 mA cm^{-2} and FF of 54.6% for *m*-xylene- and 11.6% with a V_{OC} of 0.931 V, J_{SC} of 18.7 mA cm^{-2} and FF of 66.9% for *p*-xylene-processed OSCs, respectively). The key factors of significant deterioration in the PCEs of the *m*-xylene and *p*-xylene-processed ***o*-BzY**-based devices were the lower J_{SC} and FF values, which probably originated from the unsuitable morphologies for efficient charge transport and enhanced charge recombination (*vide infra*). The relatively high V_{OC} values observed in all the ***o*-BzY**-based devices were attributed to the larger optical

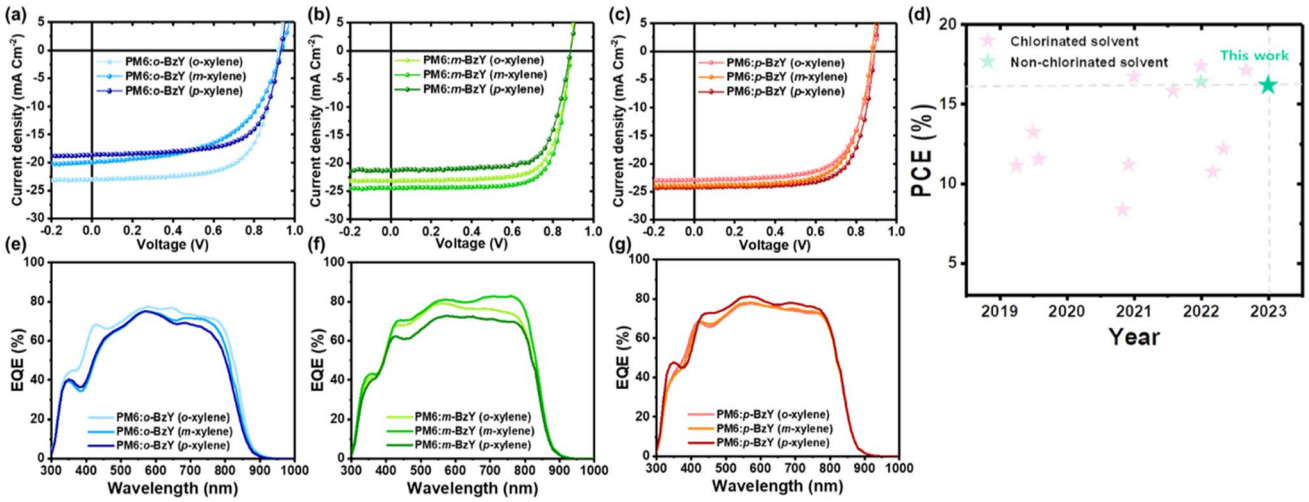

Fig. 6 *J*–*V* characteristics of (a) PM6 : ***o*-BzY**, (b) PM6 : ***m*-BzY**, and (c) PM6 : ***p*-BzY**. (d) Comparison of PCE values in the literature and this work for OSCs with a non-additive and non-annealing process (red stars for chlorinated solvent and green stars for non-chlorinated solvent). EQE spectra of (e) PM6 : ***o*-BzY**, (f) PM6 : ***m*-BzY**, and (g) PM6 : ***p*-BzY** of each optimized device.

Table 2 Summary of the photovoltaic parameters of the optimized devices under the illumination of AM1.5G (100 mW cm^{-2})

Active layer	Processing solvent	V_{OC} [V][a]	J_{SC} [mA cm^{-2}][a]	Integrated J_{SC} [mA cm^{-2}][b]	FF [%][a]	PCE [%][a]
PM6 : ***o*-BzY** (1 : 1.5)	*o*-Xylene	0.924 (0.920 ± 0.004)	22.7 (22.9 ± 0.48)	21.3	67.9 (66.5 ± 0.85)	14.2 (14.0 ± 0.23)
	m-Xylene	0.935 (0.932 ± 0.003)	20.0 (19.8 ± 0.71)	19.7	54.6 (56.1 ± 1.13)	10.2 (10.3 ± 0.23)
	p-Xylene	0.931 (0.933 ± 0.004)	18.7 (17.9 ± 0.68)	18.6	66.9 (64.4 ± 2.08)	11.6 (10.8 ± 0.66)
PM6:***m*-BzY** (1 : 1.3)	*o*-Xylene	0.881 (0.889 ± 0.002)	23.2 (22.9 ± 0.21)	21.7	74.3 (73.6 ± 0.51)	15.2 (15.2 ± 0.1)
	m-Xylene	0.888 (0.884 ± 0.004)	24.4 (24.1 ± 0.37)	23.1	74.5 (74.2 ± 0.33)	16.1 (15.8 ± 0.20)
	p-Xylene	0.886 (0.881 ± 0.014)	21.3 (21.1 ± 0.93)	20.2	72.2 (73.0 ± 1.77)	13.6 (13.6 ± 0.21)
PM6 : ***p*-BzY** (1 : 1.2)	*o*-Xylene	0.888 (0.887 ± 0.002)	22.6 (22.9 ± 0.43)	21.4	67.9 (67.2 ± 0.82)	13.6 (13.7 ± 0.24)
	m-Xylene	0.878 (0.881 ± 0.003)	23.9 (23.7 ± 0.25)	22.3	68.5 (67.6 ± 0.79)	14.4 (14.1 ± 0.15)
	p-Xylene	0.891 (0.889 ± 0.003)	24.2 (24.0 ± 0.33)	22.7	71.3 (70.2 ± 1.49)	15.4 (15.0 ± 0.40)

[a] The average values and standard deviations in the parentheses are based on 15 devices. [b] The integrated J_{SC} is calculated from EQE spectra.

bandgap of those films [*vide infra* for the external quantum efficiency (EQE) spectra and *vide supra* for the absorption spectra].[47,48] Consequently, PM6 : ***m*-BzY** processed with *m*-xylene, PM6 : ***p*-BzY** with *p*-xylene, and PM6 : ***o*-BzY** with *o*-xylene showed the best performance with higher J_{SC} and FF values. In particular, PM6 : ***m*-BzY** in *m*-xylene showed the best performance among all systems, with a maximum PCE of 16.1% with enhanced photovoltaic parameters. To the best of our knowledge, this PCE value is almost equal to the highest PCE of OSCs with non-additive, non-annealing process, and non-chlorinated solvent in the literature, as summarized in Fig. 6(d) and Table S10†.

Fig. 6(e)–(g) show the EQE. All the devices based on ***m*-BzY** and ***p*-BzY** showed higher EQEs than that of ***o*-BzY** in the entire range of 300–1000 nm. In particular, PM6 : ***m*-BzY** processed with *m*-xylene exhibited a slightly stronger response at the longer wavelength of the acceptor absorption (700–800 nm), resulting in the highest integrated J_{SC} of 23.1 mA cm^{-2}, which is consistent with the aforementioned absorption coefficient values of the BzY-series NFAs of the neat films and measured J_{SC} from the *J*–*V* curves within 5% mismatch. Table 2 lists the integrated J_{SC} values of the other devices. In addition, the devices based on *o*-xylene-processed ***o*-BzY** exhibited a higher EQE response than the *m*-xylene- and *p*-xylene-processed ones, which was attributed to the higher absorption coefficient value (*vide supra* for the absorption coefficient data).

The energy losses (E_{loss}) in the optimized devices were investigated (Fig. S11† and Table S11†). The total E_{loss} can be expressed as follows: $E_{loss} = \Delta E_{rad} + (E_g^{opt} - E_{CT}) + \Delta E_{nonrad} = \Delta E_1 + \Delta E_2 + \Delta E_3$, where ΔE_1 is ΔE_{rad}, which originated from radiative recombination above the bandgap due to the Shockley–Queisser limit. ΔE_2 is additional radiative recombination originating from the absorption below the bandgap related to the charge dynamics, which can be calculated by using $E_g^{opt} - E_{CT}$, where E_g^{opt} is the optical bandgap of the blend films from the derivatives of the EQE spectra, and E_{CT} represents the charge transfer state energy. ΔE_3 is ΔE_{nonrad}, which is related to nonradiative recombination, and can be calculated from $\Delta E_{nonrad} = -kT \ln(EQE_{EL})$, where k is the Boltzmann constant, T is the temperature in K, and EQE_{EL} is the EQE of electroluminescence (EL) when charge carriers are injected under dark

conditions.[49] Overall, the devices showed similar total energy losses. All the tested devices exhibited similar ΔE_1 values. The ΔE_2 varied depending on the applied NFAs: ***o*-BzY** displayed higher values (>0.06 eV) than ***m*-BzY**- and ***p*-BzY**-applied devices ($\approx$0.05 eV) because of the difference in E_g^{opt} derived from the EQE spectra. However, the energy losses of ***o*-BzY**-based devices were fully compensated for by the small ΔE_3 with less non-radiative recombination. Therefore, the higher V_{OC} values of the ***o*-BzY**-based devices originated from the larger optical bandgap of ***o*-BzY** than ***m*-BzY** and ***p*-BzY**, which can be reconfirmed by the crossing point between electroluminescence and EQE_{PV} spectra (Fig. S12†).[48]

Charge-carrier transport and recombination dynamics

The J_{SC} and V_{OC} were measured as a function of the light intensity (P_{light}) to delineate the main recombination mechanism of the BzY-series-based devices, as shown in Fig. 7(a)–(c). Generally, the J_{SC} dependence on P_{light} can be described as $J_{SC} \propto P_{light}{}^{\alpha}$, where the power-law exponent α is a factor related to bimolecular recombination.[50] In the PM6 : ***m*-BzY** device, a fitted α of 0.972 was obtained when it was processed with *m*-xylene, which is the nearest value to unity among the tested devices based on the synthesized NFAs. In addition, both PM6 : ***p*-BzY** devices fabricated with *p*-xylene and PM6 : ***o*-BzY** with *o*-xylene acquired α values closer to unity (0.965 and 0.961, respectively) than those in other xylene-used systems. Hence, the OSCs of PM6 : NFAs fabricated with identically oriented xylenes showed weaker bimolecular recombination, accounting for the high FF. In particular, PM6 : ***m*-BzY** showed the closest α to 1, which means the least bimolecular recombination leading to a higher FF of 74.5% and the best PCE of 16.1%.

In addition, the relationship between V_{OC} and P_{light} can be described as $V_{OC} \propto nk_BT/q \ln(P_{light})$, where k_B, T, and q are defined as the Boltzmann constant, Kelvin temperature, and elementary charge, respectively.[51] The presence of trap-assisted Shockley–Read–Hall (SRH) recombination can be related to the ideal factor (n) close to 2. The n value should be close to 1 k_BT/q if bimolecular recombination is the dominant mechanism in the device, whereas the slope should be close to 0.5 k_BT/q if surface recombination is the dominant mechanism.[52] The slopes of the PM6 : ***m*-BzY**-based devices were calculated to be 1.06 (*o*-xylene), 1.01 (*m*-xylene), and 1.20 k_BT/q (*p*-xylene). Slopes of 1.09 (*o*-xylene), 1.06 (*m*-xylene), and 1.01 k_BT/q (*p*-xylene) were obtained in the cases of ***p*-BzY** (Fig. 7(d)–(f)). Hence, bimolecular recombination is dominant in all the ***m*-BzY** and ***p*-BzY**-used cells rather than monomolecular

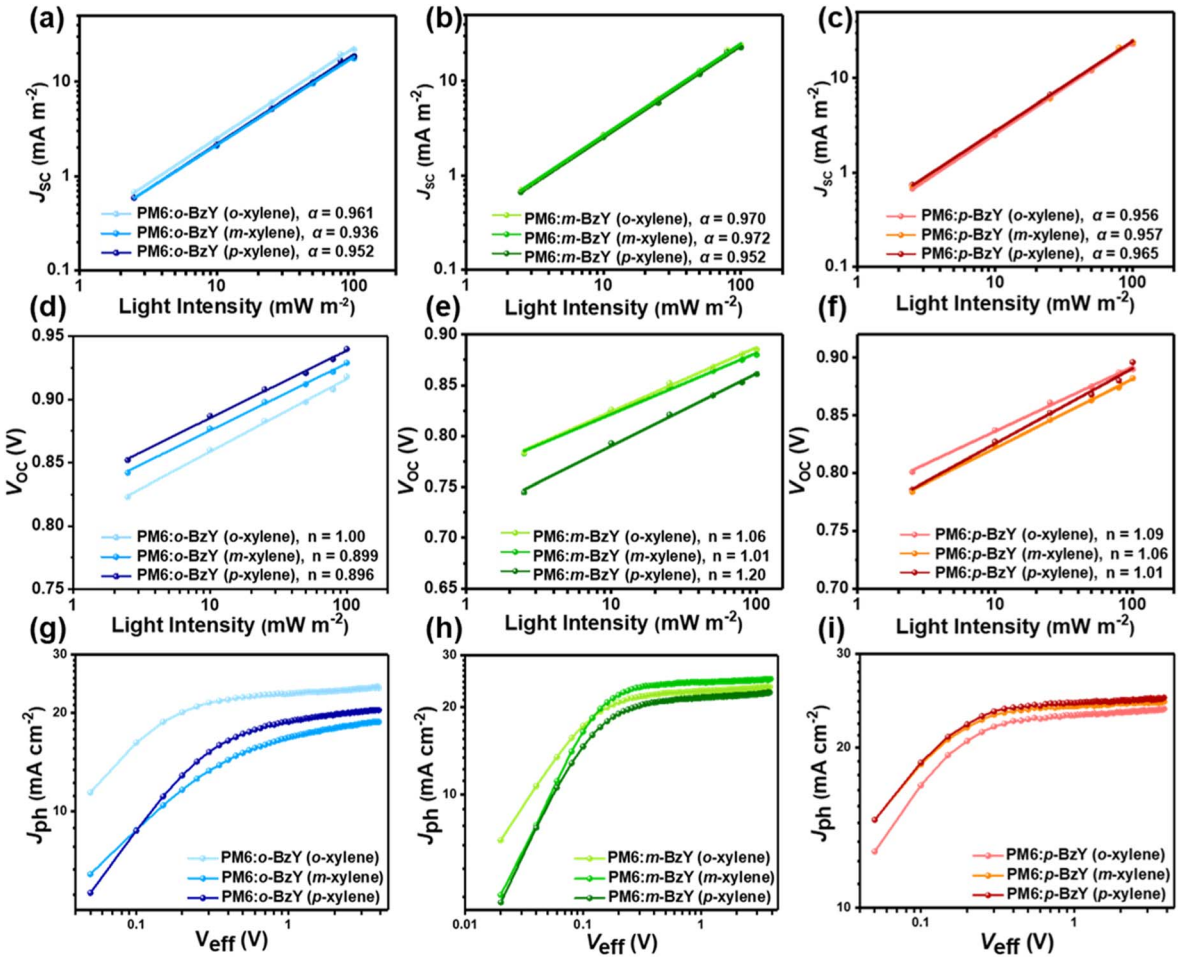

Fig. 7 Light intensity dependence of (a)–(c) J_{SC} and (d)–(f) V_{OC}, and (g)–(i) J_{ph} *versus* V_{eff} for the optimized BzY series-based devices.

recombination, particularly in the PM6 : ***m*-BzY**-based devices prepared from *m*-xylene and the PM6 : ***p*-BzY**-based devices prepared from *p*-xylene. Unlike the PM6 : ***o*-BzY**-based devices fabricated with *o*-xylene exhibiting the slopes of 1.00 k_BT/q, the *m*-xylene and *p*-xylene-processed devices show much lower slopes of 0.899 and 0.896 k_BT/q, respectively, suggesting a suppressed bimolecular recombination and increased influence of surface recombination on those devices, which is consistent with the higher roughness of those films observed by AFM (*vide infra*).[53,54]

Fig. 7(g)–(i) show the plots of the photocurrent density (J_{ph}) of the PM6 : NFA-based OSCs as a function of the effective voltage (V_{eff}). Here $V_{eff} = V_0 - V_{bias}$ and $J_{ph} = J_{light} - J_{dark}$, where V_0 is the voltage when J_{ph} is equal to zero; V_{bias} is the applied voltage; J_{light} and J_{dark} are the current density under illumination at 100 mW cm^{-2} and under dark conditions, respectively. The exciton dissociation probability (P_{diss}) and charge collection probability (P_{coll}) can be calculated by using $P_{diss} = J_{ph}/J_{sat}$ and $P_{coll} = J_{ph}/J_{sat}$, where J_{ph} is the short-circuit current condition and maximum power output, respectively.[17,55] As listed in Table S12†, the PM6 : ***p*-BzY**-based devices exhibited reasonable P_{diss} and P_{coll} values regardless of processing solvents. However, the PM6 : ***m*-BzY** and PM6 : ***o*-BzY** based OSCs showed higher values of 99.3%/89.6% in the *m*-xylene-processed devices and 98.0%/86.0% in the *o*-xylene-processed devices, respectively, compared to those in the other solvents. These results indicate better exciton dissociation and charge collection of those devices, which is well matched with the aforementioned charge recombination studies. In addition, the photoluminescence (PL) spectra of neat PM6 and BzY-series NFAs and corresponding blend films were recorded to evaluate the charge transfer properties.[56] As shown in Fig. S13,† the PL spectrum of ***m*-BzY** and ***p*-BzY**-used blend films was more effectively quenched compared to ***o*-BzY** in the range of 800–1000 nm, indicating efficient charge transfer.

Blend film morphology and microstructure analysis

AFM was performed to investigate the nanoscale morphology of the optimized blend films. The PM6 : ***o*-BzY** blend film prepared with *o*-xylene showed smooth and uniform surface morphologies with a RMS roughness of 1.12 nm (Fig. 8(a)). In contrast, *m*-xylene- and *p*-xylene-processed films displayed extremely high RMS values of 15.5 and 13.3 nm, respectively, which can be attributed to the lower solubility and higher crystalline nature of ***o*-BzY** that negatively affects charge separation and contribute to the lower EQE and J_{SC} of those devices.[23] The PM6 : ***m*-BzY** blend films showed relatively smooth surfaces: RMS roughnesses of 1.15 nm and 1.49 nm for the *o*-xylene- and *m*-xylene-processed devices, respectively. On the other hand, a relatively rougher surface with an RMS roughness of 3.04 nm was detected in the *p*-xylene-processed film, indicating a lower J_{SC} value of the corresponding devices. In the case of PM6 : ***p*-BzY** blend films, the uniform and smooth surface with RMS roughnesses of 0.963–1.13 nm in all kinds of xylene-processed ones probably influenced the ameliorated deviation of J_{SC} values of all the PM6 : ***p*-BzY**-based devices.

GIWAXS measurements were conducted to further understand the blend film molecular orientations. The blend films were prepared using each NFA (***o*-BzY**, ***m*-BzY**, and ***p*-BzY**) and PM6 donor polymer under the optimized device conditions (Fig. 8(b), S14, S15, S16, Tables S13 and S14†). For neat PM6, as shown in Fig. S14,† predominant edge-on orientation was observed in xylenes-processed films. Among the blend films, the PM6 : ***m*-BzY** films adopted a dominant face-on orientation; π–π stacking peaks in the OOP direction and lamellar stacking peaks in the IP direction were observed. In particular, the *m*-xylene-processed film reported a shorter vertical π–π staking distance of $d_{\pi-\pi}$ = 3.675 Å, indicating a tighter molecular packing structure. The PM6 : ***p*-BzY** films also exhibited

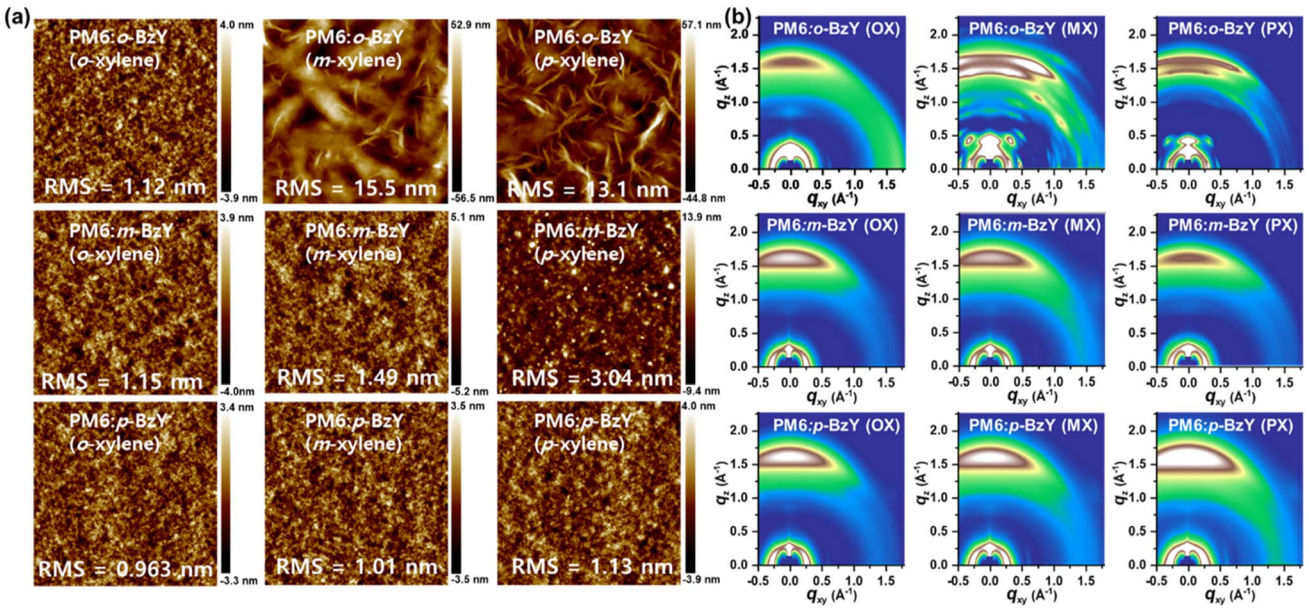

Fig. 8 (a) AFM height and (b) 2D GIWAXS images for optimized blend films.

a preferred face-on orientation. Interestingly, the PM6 : ***o*-BzY** films exhibited markedly different diffraction patterns depending on the processing solvents; only the *o*-xylene-processed film adopted a bimodal intermolecular packing structure with the coexistence of face-on and edge-on orientations. By contrast, *m*-xylene- and *p*-xylene-processed films showed randomly oriented diffraction signals for the crystallites in a large azimuthal angle range, which were attributed to the strong aggregation of ***o*-BzY** and are consistent with the AFM results. Such distinguishable packing orientation in PM6 : ***o*-BzY** blend films according to processing xylene solvents is probably due to their characteristic molecular behaviors in the film-forming process induced by the partial interaction of benzyl pendants in the solution of different kinds of isomeric xylenes. Furthermore, the miscibility between donor polymers and NFAs is considered a key factor of blend morphologies. Thus, we calculated the Flory–Huggins interaction parameter (χ) using contact angle measurement to understand the different crystalline orientation behaviors of blend films depending on the kind of xylene solvent (Fig. S17 and Table S15†). As a result, the ***o*-BzY** films exhibited higher χ values of 0.52 and 0.51 with PM6 when they were processed with *m*-xylene- and *p*-xylene, respectively, compared to the *o*-xylene-processed one of 0.15. It implies that low miscibility between ***o*-BzY** and PM6 under *m*-xylene- and *p*-xylene conditions induced the characteristic diffraction signals of the PM6 : ***o*-BzY** blend, which seem to represent the predominant packing behaviors of ***o*-BzY** itself.[57] In summary, when BzY-series NFAs are blended with a PM6 donor, ***m*-BzY** and ***p*-BzY** construct well-ordered dominant face-on orientations favorable for efficient charge transport. Moreover, ***o*-BzY** showed more suitable packing behaviors in only *o*-xylene-processed blend films for charge transport.

Remarkably, the CCL values demonstrate that the PM6 : ***m*-BzY** blend film prepared with *m*-xylene and the PM6 : ***p*-BzY** blend film prepared with *p*-xylene have a slightly higher crystallinity, exhibiting $CCL_{\pi-\pi} = 31.354$ Å and $CCL_{\pi-\pi} = 30.814$ Å in the OOP direction, respectively. At the same time, all other xylene-processed each kind of blend films exhibit almost similar values of $CCL_{\pi-\pi}$. The position of the substituted hexyl chains on the benzyl pendants in the NFAs and the film-processing isomeric xylene solvents simultaneously affects the molecular orientation and crystalline features. Consequently, three isomeric NFAs adopt favorable morphological characteristics for efficient charge transport in blend films when processed with identically oriented xylenes, *e.g.*, PM6 : ***o*-BzY** of *o*-xylene-, PM6 : ***m*-BzY** of *m*-xylene-, and PM6 : ***p*-BzY** of *p*-xylene-processed films. Among them, the PM6 : ***m*-BzY** film processed with *m*-xylene has a dominant face-on orientation, and the strongest vertical π–π stacking, leading to the highest J_{SC} and FF achieved in all the devices tested.

Conclusions

A benzene ring was introduced into the branched position of the inner side chain in Y-series NFAs to give distinctive features. Three new isomeric Y-series NFAs, ***o*-BzY**, ***m*-BzY**, and ***p*-BzY** (so-called BzY-series), were designed and synthesized by inserting the isomeric benzyl side chains distinguished by the hexyl-attached position to explore the effects of isomeric benzyl side chains and the isomerism in the inner benzyl side-chain on the intermolecular behaviors. OSCs based on three isomeric BzY-series NFAs were developed with three isomeric xylenes (*o*-xylene, *m*-xylene, and *p*-xylene) as non-chlorinated processing solvents. Through methodical studies, including theoretical calculations, optical investigations, and morphological/structural analyses, isomerism in the benzyl side chain on the BzY-series NFAs significantly affects the optical characteristics, aggregation morphologies, and crystalline properties of the corresponding films. Furthermore, the interrelationship in the pairs of isomeric NFAs and xylenes was investigated carefully *via* 1/2D-NMR spectroscopy. All the analyzed results strongly indicate that the isomeric inner benzyl side chains bring about different intermolecular behaviors. The kinds of isomeric xylene solvents can also induce different partial intermolecular interactions. The ***m*-BzY**-based films showed enhanced intermolecular packing and higher and properly well-ordered crystalline behaviors, which are suitable for efficient charge transport, particularly in the films processed with *m*-xylene. All the OSCs using synthesized BzY-series NFAs and non-chlorinated processing solvent, *o*-xylene, *m*-xylene, and *p*-xylenes with the PM6 donor exhibited their optimal photovoltaic performance without any help of additives and a thermal annealing process. Moreover, identically oriented pairs of BzY-series NFA and xylene (*i.e.*, ***o*-BzY** with *o*-xylene, ***m*-BzY** with *m*-xylene, and ***p*-BzY** with *p*-xylene)-based OSCs demonstrated higher PCE with appropriate morphologies and improved J_{SC} and FF values, compared to the devices prepared with different kinds of xylenes. These findings suggest a new approach to designing NFAs that can be utilized in additive/thermal annealing-free devices using non-chlorinated solvents for the commercialization of NFA-based OSCs and provides meaningful clues for the interrelationship between the pairs of isomeric NFAs and processing solvents.

Author contributions

S. J., J. P., and Y. J. conceived the idea and analysed the data. Y. C., B. L., M. J., S. J., and S. Y. conducted the measurements and prepared relevant figures. Y. Z. and S.-J. Y. reviewed the data. C. Y. and S. J. wrote the manuscript. C. Y. conceived and supervised the project and provided intellectual and technical guidance. All authors reviewed the manuscript.

Conflicts of interest

There are no conflicts to declare.

Acknowledgements

This work was supported by the National Research Foundation of Korea (NRF) grant funded by the Korea government (MSIP) (2021R1A2C3004202), Wearable platform Materials Technology Center (2022R1A5A6000846) funded by the Korean Government

(MSIT), Technology Development Program to Solve Climate Changes of the National Research Foundation (NRF) funded by the Ministry of Science, ICT & Future Planning (2020M1A2A2080746), Korea Institute of Energy Technology Evaluation and Planning (KETEP) grant funded by Korea government (MOTIE) (20213091010010, Super Solar cells-Development of double junction solar cells, breakthrough for the theoretical limit of silicon solar cell efficiency (>35%)), and Foreign expert project of Jilin Province (L202233).

Notes and references

1 Y. Chen, X. Wan and G. Long, *Acc. Chem. Res.*, 2013, **46**, 2645–2655.
2 B. Lee, S. Jeong, Y. Cho, M. Jeong, S. M. Lee, J. Oh and C. Yang, *Adv. Funct. Mater.*, 2020, **30**, 2005037.
3 Y. Liu, B. Liu, C.-Q. Ma, F. Huang, G. Feng, H. Chen, J. Hou, L. Yan, Q. Wei, Q. Luo, Q. Bao, W. Ma, W. Liu, W. Li, X. Wan, X. Hu, Y. Han, Y. Li, Y. Zhou, Y. Zou, Y. Chen, Y. Li, Y. Chen, Z. Tang, Z. Hu, Z.-G. Zhang and Z. Bo, *Sci. China: Chem.*, 2022, **65**, 224–268.
4 Y. Liu, B. Liu, C.-Q. Ma, F. Huang, G. Feng, H. Chen, J. Hou, L. Yan, Q. Wei, Q. Luo, Q. Bao, W. Ma, W. Liu, W. Li, X. Wan, X. Hu, Y. Han, Y. Li, Y. Zhou, Y. Zou, Y. Chen, Y. Liu, L. Meng, Y. Li, Y. Chen, Z. Tang, Z. Hu, Z.-G. Zhang and Z. Bo, *Sci. China: Chem.*, 2022, **65**, 1457–1497.
5 L. Lu, T. Zheng, Q. Wu, A. M. Schneider, D. Zhao and L. Yu, *Chem. Rev.*, 2015, **115**, 12666–12731.
6 J. Oh, S. Jung, S.-H. Kang, G. Park, M. Jeong, S. Kim, S. Lee, W. Kim, B. Lee, S. M. Lee and C. Yang, *J. Mater. Chem. A*, 2022, **10**, 20606–20615.
7 J. Hou, O. Inganäs, R. H. Friend and F. Gao, *Nat. Mater.*, 2018, **17**, 119–128.
8 C. Li, J. Zhou, J. Song, J. Xu, H. Zhang, X. Zhang, J. Guo, L. Zhu, D. Wei, G. Han, J. Min, Y. Zhang, Z. Xie, Y. Yi, H. Yan, F. Gao, F. Liu and Y. Sun, *Nat. Energy*, 2021, **6**, 605–613.
9 M. List, T. Sarkar, P. Perkhun, J. Ackermann, C. Luo and U. Würfel, *Nat. Commun.*, 2018, **9**, 3631.
10 D. Luo, W. Jang, D. D. Babu, M. S. Kim, D. H. Wang and A. K. K. Kyaw, *J. Mater. Chem. A*, 2022, **10**, 3255–3295.
11 J. Yuan, Y. Zhang, L. Zhou, G. Zhang, H.-L. Yip, T.-K. Lau, X. Lu, C. Zhu, H. Peng, P. A. Johnson, M. Leclerc, Y. Cao, J. Ulanski, Y. Li and Y. Zou, *Joule*, 2019, **3**, 1140–1151.
12 Y. Wei, Z. Chen, G. Lu, N. Yu, C. Li, J. Gao, X. Gu, X. Hao, G. Lu, Z. Tang, J. Zhang, Z. Wei, X. Zhang and H. Huang, *Adv. Mater.*, 2022, **34**, 2204718.
13 L. Zhu, M. Zhang, J. Xu, C. Li, J. Yan, G. Zhou, W. Zhong, T. Hao, J. Song, X. Xue, Z. Zhou, R. Zeng, H. Zhu, C.-C. Chen, R. C. I. MacKenzie, Y. Zou, J. Nelson, Y. Zhang, Y. Sun and F. Liu, *Nat. Mater.*, 2022, **21**, 656–663.
14 C. Kim, S. Chen, J. S. Park, G.-U. Kim, H. Kang, S. Lee, T. N.-L. Phan, S.-K. Kwon, Y.-H. Kim and B. J. Kim, *J. Mater. Chem. A*, 2021, **9**, 24622–24630.
15 S. Lee, G. Park, M. Jeong, B. Lee, S. Jeong, J. Park, Y. Cho, S. M. Noh and C. Yang, *ACS Appl. Mater. Interfaces*, 2022, **14**, 33614–33625.
16 G. Li, X. Zhang, L. O. Jones, J. M. Alzola, S. Mukherjee, L.-W. Feng, W. Zhu, C. L. Stern, W. Huang, J. Yu, V. K. Sangwan, D. M. DeLongchamp, K. L. Kohlstedt, M. R. Wasielewski, M. C. Hersam, G. C. Schatz, A. Facchetti and T. J. Marks, *J. Am. Chem. Soc.*, 2021, **143**, 6123–6139.
17 G. Chai, Y. Chang, J. Zhang, X. Xu, L. Yu, X. Zou, X. Li, Y. Chen, S. Luo, B. Liu, F. Bai, Z. Luo, H. Yu, J. Liang, T. Liu, K. S. Wong, H. Zhou, Q. Peng and H. Yan, *Energy Environ. Sci.*, 2021, **14**, 3469–3479.
18 Y. Cui, H. Yao, J. Zhang, K. Xian, T. Zhang, L. Hong, Y. Wang, Y. Xu, K. Ma, C. An, C. He, Z. Wei, F. Gao and J. Hou, *Adv. Mater.*, 2020, **32**, 1908205.
19 K. Jiang, Q. Wei, J. Y. L. Lai, Z. Peng, H. K. Kim, J. Yuan, L. Ye, H. Ade, Y. Zou and H. Yan, *Joule*, 2019, **3**, 3020–3033.
20 C. McDowell and G. C. Bazan, *Curr. Opin. Green Sustainable Chem.*, 2017, **5**, 49–54.
21 D. Wang, G. Zhou, Y. Li, K. Yan, L. Zhan, H. Zhu, X. Lu, H. Chen and C.-Z. Li, *Adv. Funct. Mater.*, 2022, **32**, 2107827.
22 X. Xu, L. Yu, H. Yan, R. Li and Q. Peng, *Energy Environ. Sci.*, 2020, **13**, 4381–4388.
23 S. Dong, T. Jia, K. Zhang, J. Jing and F. Huang, *Joule*, 2020, **4**, 2004–2016.
24 P. Gopikrishna, H. Choi, D. H. Kim, J. H. Hwang, Y. Lee, H. Jung, G. Yu, T. B. Raju, E. Lee, Y. Lee, S. Cho and B. Kim, *Chem. Sci.*, 2021, **12**, 14083–14097.
25 S. J. Sung, J. Im, G. Kim, C. S. Moon, J. J. Yoo, S. S. Shin, N. J. Jeon, B. S. Ma, D. J. Kim, T.-S. Kim and J. Seo, *Adv. Energy Mater.*, 2022, **12**, 2200758.
26 S.-J. Yoon, J. W. Chung, J. Gierschner, K. S. Kim, M.-G. Choi, D. Kim and S. Y. Park, *J. Am. Chem. Soc.*, 2010, **132**, 13675–13683.
27 K. Koperwas, K. Adrjanowicz, A. Grzybowski and M. Paluch, *Sci. Rep.*, 2020, **10**, 283.
28 R. Khatua, S. Debata and S. Sahu, *New J. Chem.*, 2020, **44**, 8412–8421.
29 J. Bertrandie, J. Han, C. S. P. De Castro, E. Yengel, J. Gorenflot, T. Anthopoulos, F. Laquai, A. Sharma and D. Baran, *Adv. Mater.*, 2022, **34**, 2202575.
30 J. Sworakowski, J. Lipiński and K. Janus, *Org. Electron.*, 2016, **33**, 300–310.
31 Q. An, F. Zhang, L. Li, J. Wang, Q. Sun, J. Zhang, W. Tang and Z. Deng, *ACS Appl. Mater. Interfaces*, 2015, **7**, 3691–3698.
32 Y. Cui, H. Yao, J. Zhang, T. Zhang, Y. Wang, L. Hong, K. Xian, B. Xu, S. Zhang, J. Peng, Z. Wei, F. Gao and J. Hou, *Nat. Commun.*, 2019, **10**, 2515.
33 J. Ko, J. Kim, H.-J. Song, Y. Park, J. Kwak, C. Lee and K. Char, *Adv. Mater. Interfaces*, 2021, **8**, 2100029.
34 D. Qian, L. Ye, M. Zhang, Y. Liang, L. Li, Y. Huang, X. Guo, S. Zhang, Z. a. Tan and J. Hou, *Macromolecules*, 2012, **45**, 9611–9617.
35 H. Zhao, H. B. Naveed, B. Lin, X. Zhou, J. Yuan, K. Zhou, H. Wu, R. Guo, M. A. Scheel, A. Chumakov, S. V. Roth, Z. Tang, P. Müller-Buschbaum and W. Ma, *Adv. Mater.*, 2020, **32**, 2002302.
36 S. Chatterjee, T. Ohto, H. Tada, S. Jinnai and Y. Ie, *ACS Sustainable Chem. Eng.*, 2020, **8**, 19013–19022.

37 Z. Fei, P. Boufflet, S. Wood, J. Wade, J. Moriarty, E. Gann, E. L. Ratcliff, C. R. McNeill, H. Sirringhaus, J.-S. Kim and M. Heeney, *J. Am. Chem. Soc.*, 2015, **137**, 6866–6879.
38 J. Lee, S.-J. Ko, H. Lee, J. Huang, Z. Zhu, M. Seifrid, J. Vollbrecht, V. V. Brus, A. Karki, B. R. Luginbuhl, H. Wang, K. Cho, T.-Q. Nguyen and G. C. Bazan, *ACS Energy Lett.*, 2019, **4**, 1732.
39 S. Park, M. H. Lee, K. S. Ahn, H. H. Choi, J. Shin, J. Xu, J. Mei, K. Cho, Z. Bao, D. R. Lee, M. S. Kang and D. H. Kim, *Adv. Funct. Mater.*, 2016, **26**, 4627–4634.
40 D. Dutta, N. Nagapradeep, H. Zhu, M. Forsyth, S. Verma and A. J. Bhattacharyya, *Sci. Rep.*, 2016, **6**, 24499.
41 L. Avram and Y. Cohen, *Chem. Soc. Rev.*, 2015, **44**, 586–602.
42 D. Li, G. Kagan, R. Hopson and P. G. Williard, *J. Am. Chem. Soc.*, 2009, **131**, 5627–5634.
43 Y. Zhang, C. Yu, T. Shan, Y. Chen, Y. Wang, M. Xie, T. Li, Z. Yang and H. Zhong, *Cell Rep. Phys. Sci.*, 2022, **3**, 100765.
44 S. Zhang, Y. Qin, J. Zhu and J. Hou, *Adv. Mater.*, 2018, **30**, 1800868.
45 Y. Liu, M. Li, J. Yang, W. Xue, S. Feng, J. Song, Z. Tang, W. Ma and Z. Bo, *Adv. Energy Mater.*, 2019, **9**, 1901280.
46 X. Xu, Y. Qi, X. Luo, X. Xia, X. Lu, J. Yuan, Y. Zhou and Y. Zou, *Fundam. res.*, 2022, DOI: **10.1016/j.fmre.2022.01.025**.
47 L. Perdigón-Toro, L. Q. Phuong, F. Eller, G. Freychet, E. Saglamkaya, J. I. Khan, Q. Wei, S. Zeiske, D. Kroh, S. Wedler, A. Köhler, A. Armin, F. Laquai, E. M. Herzig, Y. Zou, S. Shoaee and D. Neher, *Adv. Energy Mater.*, 2022, **12**, 2103422.
48 K. Vandewal, J. Benduhn and V. C. Nikolis, *Sustain. Energy Fuels*, 2018, **2**, 538–544.
49 D. He, F. Zhao, C. Wang and Y. Lin, *Adv. Funct. Mater.*, 2022, **32**, 2111855.
50 S. R. Cowan, A. Roy and A. J. Heeger, *Phys. Rev. B: Condens. Matter Mater. Phys.*, 2010, **82**, 245207.
51 W. Xu, X. Zhu, X. Ma, H. Zhou, X. Li, S. Y. Jeong, H. Y. Woo, Z. Zhou, Q. Sun and F. Zhang, *J. Mater. Chem. A*, 2022, **10**, 13492–13499.
52 S. Solak, A. G. Ricciardulli, T. Lenz, N. I. Crăciun, P. W. M. Blom and G. A. H. Wetzelaer, *Appl. Phys. Lett.*, 2017, **110**, 163301.
53 J. Ge, L. Xie, R. Peng, B. Fanady, J. Huang, W. Song, T. Yan, W. Zhang and Z. Ge, *Angew. Chem., Int. Ed.*, 2020, **59**, 2808–2815.
54 S. Wheeler, F. Deledalle, N. Tokmoldin, T. Kirchartz, J. Nelson and J. R. Durrant, *Phys. Rev. Appl.*, 2015, **4**, 024020.
55 T. Wang, X.-Y. Yang, P.-Q. Bi, M.-S. Niu, L. Feng, J.-Q. Liu and X.-T. Hao, *Solar RRL*, 2019, **3**, 1900087.
56 T. A. Shastry, I. Balla, H. Bergeron, S. H. Amsterdam, T. J. Marks and M. C. Hersam, *ACS Nano*, 2016, **10**, 10573–10579.
57 F. T. A. Wibowo, N. V. Krishna, S. Sinaga, S. Lee, W. T. Hadmojo, Y. R. Do and S.-Y. Jang, *Cell Rep. Phys. Sci.*, 2021, **2**, 100517.

